Radiation Enhanced Anion Diffusion in Chromia

Yano, Kayla
Kohnert, Aaron Anthony
Kaspar, Tiffany
Taylor, Sandra
Spurgeon, Steven
Kim, Hyosim
Wang, Yongqiang
Uberuaga, Blas P.
Schreiber, Daniel

To be published in: The Journal of Physical Chemistry C

DOI to publisher's version: 10.1021/acs.jpcc.1c08705

Radiation Enhanced Anion Diffusion in Chromia

Kayla H. Yano[*1], Aaron A. Kohnert[2], Tiffany C. Kaspar[3], Sandra D. Taylor[3], Steven R. Spurgeon[1], Hyosim Kim[2], Yongqiang Wang[2], Blas P. Uberuaga[2], Daniel K. Schreiber[1]*

[1]Energy & Environment Directorate, Pacific Northwest National Laboratory, Richland, WA, 99354, USA

[2]Material Science and Technology Division, Los Alamos National Laboratory, Los Alamos, NM, 87545, USA

[3]Physical and Computational Sciences Directorate, Pacific Northwest National Laboratory, Richland, WA, 99354, USA

AUTHOR INFORMATION

Kayla H. Yano*

*Contact information: kayla.yano@pnnl.gov, (509)-375-2833

ABSTRACT

Cr_2O_3 is a ubiquitous passivating film on alloys that is vital to their stability and performance in hostile environments. In this study, we directly observe and measure how anion transport through the oxide is affected by 400 keV Ar^{2+} ion irradiation as a function of temperature (30 to 500 °C) and dose (0.33 to 2.00 dpa) in single-crystal Cr_2O_3 films using embedded ^{18}O isotopic tracers and atom probe tomography. Diffusion coefficients are experimentally determined and compared to a chemical-rate theory model. Experimental and theoretical results are broadly in agreement, showing anion diffusion increases at least 4–5 orders of magnitude upon irradiation with a weak dependence on temperature and a stronger dose-driven sink-strength dependence. These results reveal that radiation could significantly reduce the protectiveness of Cr_2O_3 films when passivity relies upon limited anion diffusivity, even at relatively modest levels of irradiation and low temperatures.

TOC GRAPHICS

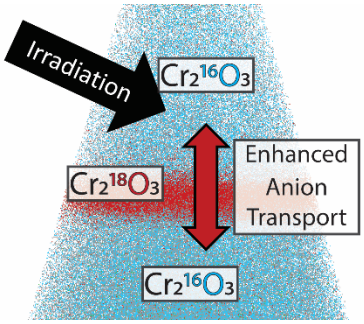

KEYWORDS chromia, anion diffusion, isotopic tracers, ion irradiation, atom probe tomography, scanning transmission electron microscopy, chemical rate theory

INTRODUCTION

Oxidation and corrosion of structural alloys in high-temperature hostile environments, commonly found in energy-generating systems, impact material reliability and performance, resulting in costly component repairs, replacement, or even catastrophic failure. The natural formation of a nanoscale passivating oxide layer on an alloy surface can aid in mitigating material degradation in many oxidizing environments.[1] Nuclear reactors create a unique challenge for corrosion resistance because radiation introduces high densities of point defects and structural flaws into both the protective oxide film and underlying metal.[2] These point and extended defect structures inherently alter both the properties of the oxide film and its ability to reform should it rupture or spall. Understanding the underlying atomic transport within protective oxide layers under irradiation is thus of great importance for designing materials that must exhibit both corrosion resistance and radiation tolerance.

Chromia (Cr_2O_3), a common passivating film for Ni- and Fe-based alloys, effectively eliminates ion transport and further corrosion of the underlying metal (in the absence of radiation) via very thin layers (2–5 nm thickness). Isotopic tracers, e.g. ^{18}O, have been used to generate fundamental insights into oxidation mechanisms and rates for chromia on alloys using mass-sensitive analytical techniques.[3–5] For example, the growth of Cr_2O_3 films has been studied on Fe-Cr[6,7] and Ni-Cr[8] alloys, where two-stage oxidation with first natural isotopic abundance and then ^{18}O-enriched gas from the oxidizing environment can reveal the competition between the inward penetration of ^{18}O anions and outward migration of metal cations. While these two-stage studies have not identified a definitive rate limiting mechanism, they emphasize the importance of anion transport in the development of Cr_2O_3 films. Previous studies of ion transport in bulk and

spherical (90 and 120 μm diameter) Cr_2O_3 used gas-solid reactions and secondary ion mass spectrometry (SIMS) to measure the penetration depths and rates of ^{18}O into the oxide at high temperatures (900–1400 °C).[9–11] Studies with bulk polycrystalline samples (850–1100 °C) also revealed faster diffusion (4–5 orders of magnitude) along grain boundaries than the bulk.[12,13] Likewise, experimental data on cation diffusion in Cr_2O_3 exists at high temperatures (1100-1570°C)[9,14,15] with diffusion coefficients ranging from 2×10^{-22} - 3×10^{-17} m^2/s. Computational studies suggest a high level of anisotropy in cation transport in Cr_2O_3.[16] However in this study, focus is placed only on anion transport parallel to the c-axis.

A significant lack of knowledge on the nature and behavior of chromia persists at conditions relevant to nuclear environments, such as the impact of irradiation on the oxide microstructure and rate-limiting atomic transport mechanisms and kinetics. Irradiation in oxides such as Cr_2O_3 results in the production of point defects. These point defects are a mixture of self-interstitial and vacancy defects (together referred to as Frenkel pairs) that can diffuse through the bulk crystal and recombine, reach pre-existing sinks (such as existing higher-dimension defects), or aggregate with each other to nucleate larger defects such as voids and dislocation loops, which can in turn act as defect sinks.[17,18] Defects in oxides have additional complications due to the presence of multiple sublattices and the potential for formation of charged defects.[19–21] The supersaturation of point defects introduced through irradiation can accelerate atomic diffusion, a phenomenon known as radiation-enhanced diffusion (RED).[22,23]

An Arrhenius extrapolation to 500 °C (typical temperature in an advanced reactor) and 300 °C (lightwater reactor) of thermal diffusion in Cr_2O_3 using an expression from Hagel[10] results in anion diffusivities of 4.5×10^{-32} and 4.7×10^{-42} m^2/s, respectively. Even after 100 years in service,

the characteristic anion diffusion distance ($\sqrt{4Dt}$) with these phenomenally low diffusivities would still be less than a single unit cell of Cr_2O_3. Even at higher temperatures where diffusivities increase, Cr_2O_3 (2.6×10^{-22} m^2/s at 900 °C)[11] exhibits orders of magnitude slower anion mobility than α-Fe_2O_3 (4.4×10^{-20} m^2/s at 900 °C)[24–26] and Fe_3O_4 (2.4×10^{-19} m^2/s at 800 °C).[27] However, our recent work on proton irradiated α-Fe_2O_3 demonstrated that the non-equilibrium point defect density can enhance diffusivity by at least two orders of magnitude via RED.[22] A similar increased ion diffusivity in Cr_2O_3 via RED may be detrimental to its passivating ability under dynamic irradiation in corrosive reactor environments.

In this study, we investigate both the microstructural evolution of and anion transport within epitaxial Cr_2O_3 thin films containing embedded ^{18}O isotopic tracers irradiated with heavy ions at reactor-relevant temperatures (300–500 °C). Building on our previous work with α-Fe_2O_3 films,[22,28] deposition of a well-defined ^{18}O tracer layer within a single-crystalline Cr_2O_3 film is achieved via molecular beam epitaxy (MBE). The embedded tracer layer enables us to focus on self-diffusion of O directly within the model oxide film itself, bypassing gas/solid interactions[29,30] and metal reactivity[31] that can complicate isotope diffusion profiles in traditional studies. Microstructural characterization is done using scanning/transmission electron microscopy (S/TEM), while direct visualization and quantification of atomic-level isotope diffusion via the ^{18}O tracer is accomplished using atom probe tomography (APT).[32] Experimental measurements are then coupled with previous density functional theory (DFT) modeling work[33,34] on defect energetics in Cr_2O_3 to consider both formation and migration energies of vacancy and interstitial defects. These energetics are combined into a chemical rate-theory model[22] where the self-diffusion coefficient for thermally-activated and irradiated Cr_2O_3 at varying dose and temperature can be predicted.

METHODS

Isotopically labeled layers with natural abundance oxygen (^{NA}O - 99.8% ^{16}O) and ^{18}O-enriched (99% ^{18}O) Cr_2O_3 were deposited by MBE at 730°C on sapphire (α-Al2O3) [0001] 10 × 10 mm substrates, as described previously.[28] Thicknesses (starting from the interface with the Al_2O_3 substrate) were 35 nm $Cr_2{}^{NA}O_3$, 10 nm $Cr_2{}^{18}O_3$, and 45 nm $Cr_2{}^{NA}O_{3,}$, respectively, as schematically illustrated in Fig. 1 The dimensions of the MBE films (~100 nm thick) are also convenient for heavy ion irradiation studies of RED without a requirement for high-energy irradiation and associated sample radioactivity. The growth rate was 0.1 Å/s at a substrate temperature of 730 °C. Using magnetron sputter deposition at room temperature, 2 nm Cr and 18 nm Ni were laid as a protective cap and assists in APT and TEM sample preparation via focused ion beam (FIB) methods.[35]. Before anneal and irradiation, samples were sectioned into four 5 × 5 mm rectangles.

The irradiation was conducted at the Ion Beam Materials Laboratory at Los Alamos National Laboratory. 400 kV Ar^{2+} irradiation (vacuum - 4×10^{-5} Pa) was conducted using a Danfysik implanter with a dose rate of 2×10^{-4} displacements per atom per second (dpa/s) at a 4 cup current of 165-180 nA with a rastered beam with frequencies of approximately 1kHz in both horizontal and vertical directions. Fluence varied from 9.23×10^{14} to 5.54×10^{15} ions/cm^2. Irradiations were conducted at room temperature (RT) (~30 °C with beam heating), 300 °C, or 500 °C to nominal doses of 0.33, 0.66, or 2.00 dpa, as calculated by SRIM[36]. SRIM parameters are provided in the SI. A picture of the sample with an overlaid schematic of the irradiation is included in the supplemental material, along with a cooling curve for the 500 °C specimen.

One 5 × 5 mm section of the deposited film was placed into a Thermo Scientific Thermolyne Model # FB1415M furnace for a 1000 hr anneal at 500 °C in air as an unirradiatied, control specimen. The sample was loaded into and removed from the furnace at temperature and air cooled.

Samples were prepared for S/TEM and APT using either an FEI Quanta 3D-FEG or Helios NanoLab dual-beam focused ion beam (FIB) / scanning electron microscope (SEM) system. Specimens were prepared using established procedures.[35,37] APT specimens were annularly milled at 30 kV Ga+ down to diameters of 150 nm, then polished at 2 kV Ga+ to a diameter of ~100 nm. TEM lamella were thinned using progressive steps at 30 kV, 5 kV and 2 kV Ga+.

S/TEM characterization was conducted using a JEOL JEM-ARM 200CF at 200 kV and a JEOL GrandARM-300F at 300 kV. S/TEM high-angle annular dark field images were collected with a probe size of 1.06 Å, a convergence angle of 27.5 mrad, and collection angles of 68–280 mrad. Dislocation imaging was conducted off the $[\bar{1}\bar{1}20]$ zone axis with tilts of 5–10° towards the [0001] direction with a probe size of 1.7 Å, a convergence angle of 6.9 mrad, and collection angles of 6.8-28 mrad to maximize dislocation contrast and minimize bend contours.[38]

APT specimens were analyzed with a CAMECA local electrode atom probe (LEAP) 4000X HR at a base temperature of 40 K and a pressure of $< 2.7 \times 10^{-9}$ Pa. Samples were analyzed using laser-assisted field evaporation (λ=355 nm) at pulse rates of 200 and 250 kHz and a pulse energy of 60 pJ. Detection rates were kept at 0.003 detected ions per pulse by varying the applied voltage. Data were reconstructed in 3D using the Integrated Visualization and Analysis Software (IVAS 3.8.5a45) developed by CAMECA. Since films were epitaxially grown on Al_2O_3 (0001) substrates, the (0001) pole was captured during APT, and reconstructions were scaled using the

bilayer-to-bilayer spacing of chromia along [0001] (2.3 Å) within the APT data (Fig. S6-S7).[39] This was best achieved using the voltage reconstruction method (see SI for details). Representative spectra (Fig. S4), the comparison between ^{18}O enriched and NA chromia layers (Fig. S5), and a representative 1D concentration profile (Fig. S8) are provided in the Supporting Information document. Stoichiometry of the Cr_2O_3 films is 2:3 Cr to O in the natural abundance, ^{16}O regions of the growth, consistent with prior APT studies.[40] Additional f_{18O} profiles are included in Fig. S9-S11.

Theoretical predictions for the supersaturation densities of point defects under irradiation were based on a rate theory model,[41]

$$\frac{dc_i}{dt} = \phi - D_i k_i^2 (c_i - c_i^0) - k_{iv} c_i c_v$$

$$\frac{dc_v}{dt} = \phi - D_v k_v^2 (c_i - c_v^0) - k_{iv} c_i c_v$$

evaluated at steady state, with ϕ the defect production rate, $D_{i/v}$ the defect diffusivities, k^2 the sink strength and k_{iv} the recombination coefficient for vacancies v and self-interstitials i. Self-diffusion included both vacancy and self-interstitial contributions

$$D = D_v c_v + D_i c_i$$

with defect diffusivities given by

$$D_x = D_0 \exp \frac{-E_x^m}{kT}$$

using migration energies E^m derived from density functional theory.[33,34] Thermal equilibrium densities were determined as

$$c_i^0 = \exp\frac{S_x^f}{k}\exp\frac{-H_x^f}{kT}$$

with formation enthalpies H^f from the same DFT studies, and a temperature dependent contribution to S^f and H^f from the chemical potential of O_2 at standard pressure.

RESULTS

Fig. 1 shows S/TEM bright field images comparing (A) the as-grown sample and (B-E) samples irradiated to (B,C) 0.66 dpa or (D,E) 2 dpa at either RT or 500 °C. The as-deposited Cr_2O_3 layer film is uniformly 90 nm thick with a low density of vertical threading dislocations; no other defects (e.g., voids or grain boundaries) were found. The isotopically enriched $Cr_2{}^{18}O_3$ tracer layer is indistinguishable from the surrounding $Cr_2{}^{NA}O_3$, and its approximate position is noted by white dashed lines. The $Cr_2{}^{NA}O_3$ layer deposited "below" the ^{18}O-enriched ($Cr_2{}^{18}O_3$) and closer to the Al_2O_3 substrate is labeled "$Cr_2{}^{NA}O_3$-b", and conversely "$Cr_2{}^{NA}O_3$-a" for the layer "above" the $Cr_2{}^{18}O_3$. After irradiation, dislocation loops were prevalent throughout the Cr_2O_3 film, with a ~20 nm denuded region near the interface with the metal capping layer. Loops were larger (>5 nm diameter) after irradiation at 500 °C than at RT (2–4 nm diameter). Estimates of loop number density for the 2 dpa samples were 7.5×10^{22} m^{-3} (or 75,000 μm^{-3}) at RT and 6.0×10^{22} m^{-3} (60,000 μm^{-3}) at 500°C. No corresponding nanoscale composition changes were observed in the APT analysis, suggesting the dislocation loops do not significantly affect local oxide chemistry. Vertical dislocations remained in the films, but their density decreased noticeably in both 500 °C samples. There were no observable voids or phase transformations as a result of irradiation. While ballistic mixing between the metal cap and the oxide film is a concern, the Ni cap remained intact in the S/TEM images. Potential ballistic mixing is discussed further in the APT

results below. The presence of S/TEM-visible defects (dislocation loops) demonstrates that the radiation-induced generation, supersaturation and aggregation of point defects within the film can accelerate defect-mediated atomic diffusion well beyond thermal diffusion alone and act as evolving sinks that can further modify the defect distributions within the material.

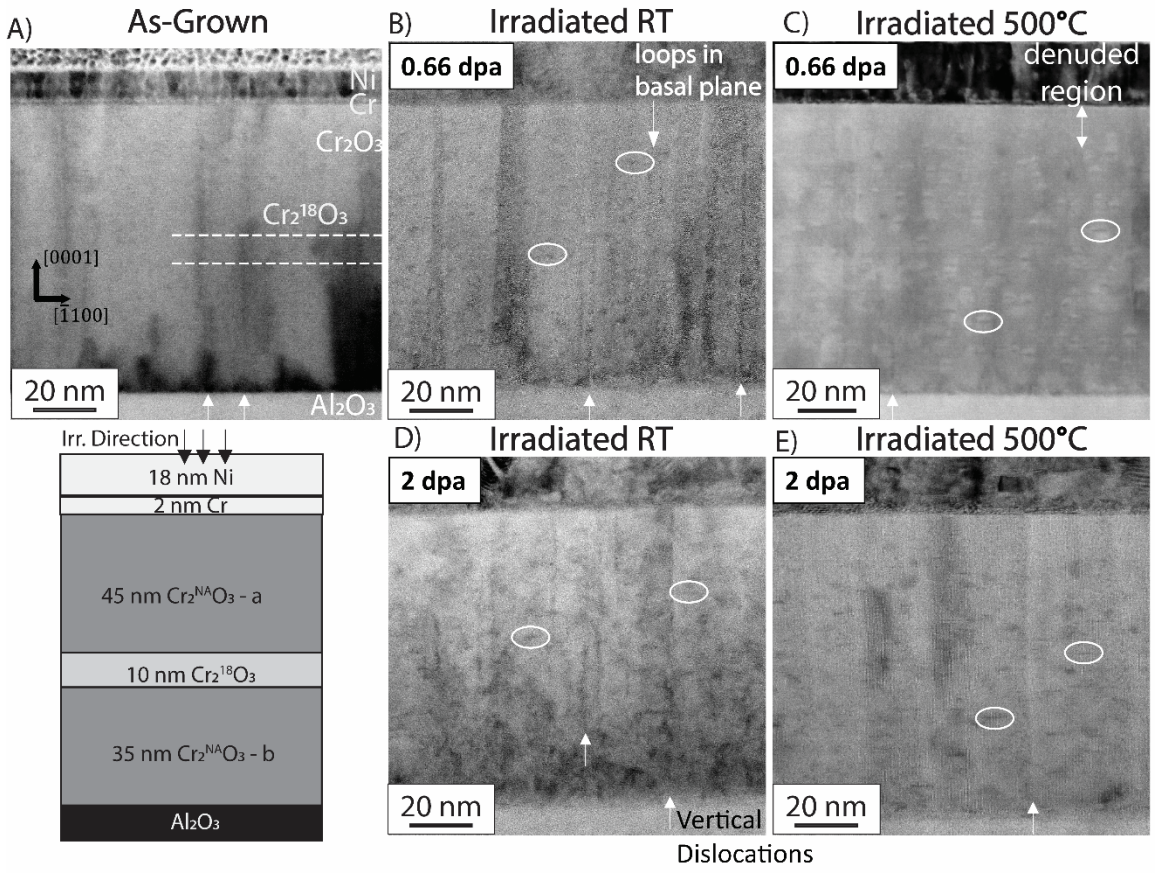

Figure 1. S/TEM bright field images of A) the as-grown Cr_2O_3 film and B-D) the same film after irradiation at (B,D) room temperature or (C,E) 500 °C. The MBE-deposited stack schematic with nominal layer thicknesses is provided at lower left. The top row of images show samples irradiated to 0.66 dpa, while those in the bottom row were irradiated to 2 dpa. Select defects have been highlighted in each image – dislocation loops with white ellipses and vertical dislocations with white arrows. Note that the loops increase in size with dose and temperature, while the vertical dislocation density reduces with temperature. Dashed white lines indicate the approximate location of the ^{18}O tracer layer, which is not visible by S/TEM imaging.

The redistribution of the ^{18}O isotopic tracer was studied using APT, which provides the necessary mass sensitivity and sub-nm spatial resolution to resolve atomic-scale ion transport. 1D

concentration profiles were taken from cylindrical regions of interest (20 nm in diameter) that spanned the entire APT specimen length, with the long axis of the cylinder perpendicular to the ^{18}O layer. Profiles of the local ^{18}O redistribution was quantified using the ^{18}O isotopic fraction (f_{18O}) (Eqn. 1):

$$f_{18O} = N_{^{18}O^{1+}} / (N_{^{18}O^{1+}} + N_{^{16}O^{1+}}) \quad (1)$$

where $N_{^{18}O}$ and $N_{^{16}O}$ denote the counts of $^{16}O^{1+}$ and $^{18}O^{1+}$, respectively.[22,28] Diffusion coefficients were extracted from the average of two f_{18O} profiles measured for each sample by numerically aging the as-grown profile via Fick's Law until the difference between the numerically aged and experimentally measured profiles is minimized. Further details on the APT methodology and this fitting procedure are found in the SI and Ref.[22]. Table 1 summarizes the resulting diffusion coefficients for each irradiation and annealing condition. Each measurement will be discussed in sequence below, but first we seek to clarify sources of error and limitations of these fittings. Two sources of uncertainty contribute to the error interval (D_{min} and D_{max} range) reported in Table 1. The first is the standard deviation of the mean of diffusivity collected from the full set of samples. The second is the confidence interval of the numerical aging, bounded by the diffusivity values where the square residual increases over the best fit by a factor of two. Note that in the case of the thermal anneal, this interval extends to zero diffusion. The final column also reports an estimate of the smallest diffusivity (D_{limit}) that the APT measurement itself could resolve.

Table 1. Summary of irradiation temperature, dose, irradiation or annealing times, and extracted anion diffusion coefficients (D) with uncertainty intervals (D_{min} and D_{max}). The estimated APT resolution limit (D_{limit}) for each condition is also shown, with an assumed 0.5 nm resolution limit – see SI.

Temperature (°C)	Dose (dpa)	Time (min)	D (10^{-22} m^2/s)	D_{min} (10^{-22} m^2/s)	D_{max} (10^{-22} m^2/s)	APT D_{limit} (10^{-22} m^2/s)
30	0.66	45	0.68	0.22	1.5	0.23
300	0.66	45	1.5	0.89	2.3	0.23
500	0.66	48	3.6	2.8	4.7	0.22
500	thermal anneal	60,000	5.9×10^{-5}	0	6.6×10^{-4}	1.7×10^{-4}
500	0.33	22	4.5	3.3	5.9	0.47
500	0.66	48	3.6	2.8	4.7	0.22
500	2.00	133	2.2	1.4	3.1	0.078
500	0.33 to 0.66	26	3.1	1.6	4.9	0.40
500	0.66 to 2.00	85	1.2	0.33	2.5	0.12

The APT reconstruction can achieve a spatial resolution in depth on the order of the oxygen bilayer spacing in Cr_2O_3 (~0.23 nm – see SI Fig. S6). To be conservative, it can be assumed that APT can achieve 0.5 nm resolution in depth for the corresponding f_{18O} profiles used to quantify the interdiffusion. If we can approximate that to be the detectable limit, the characteristic diffusion distance ($x = \sqrt{4Dt}$) should be equal to or greater than the APT spatial resolution limit (~0.5 nm conservatively), where D is the diffusion coefficient and t the diffusion time. Using this relationship, we can establish rough bounds for combinations of diffusivity and diffusion times that can be readily detected and quantified by APT. These bounds, for a few assumed resolution limits, are presented in Fig. 2 and overlayed with the experimental measurements reported in this study. While most datapoints reside well into the easily resolvable range, two datapoints exist near the resolution limit lines. These correspond to the RT irradiation to 0.66 dpa (open circle) and the 1000 h 500°C thermal anneal (open triangle). The thermal anneal datapoint clearly sits below our conservative 0.5 nm resolution limit line, indicating that no measurable diffusion has occurred. Conversely the 0.66 dpa RT anneal sits roughly a factor of 2 above our 0.5 nm resolution limit line. This indicates that APT has detected some change in f_{18O} profile that is within our experimental limits.

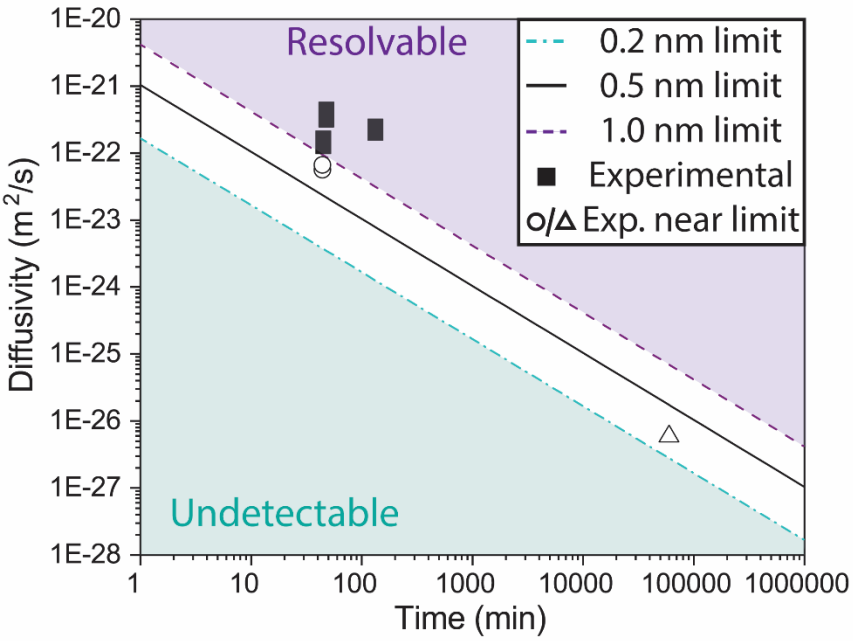

Figure 2. Effect of estimated APT spatial resolution limits with experimentally resolvable diffusivities as a function of diffusion time.

The APT-measured f_{18O} profiles of the as-grown, unirradiated 500 °C annealed, and 500 °C irradiated datasets are shown in Fig. 3. The irradiated datasets include 0.33, 0.66, and 2 dpa samples. The as-grown profiles (Fig. 3A) depict a well-defined ~10 nm thick ^{18}O enriched layer with sharp interfaces and a peak enrichment of f_{18O} ~0.9. Both the $Cr_2{}^{18}O_3$ and $Cr_2{}^{NA}O_3$-a regions exhibit gradients in the f_{18O}, suggesting some intermixing of O with the underlying film during film deposition. Because the diffusion coefficients are extracted by numerically aging the as-grown f_{18O} profile, the profile shape does not strongly affect the subsequent diffusion coefficient quantification. Profiles from two APT specimens are included to demonstrate the repeatability of these measurements. To rule out pure thermal contributions to anion diffusion during irradiation, a section of the wafer was annealed in air at 500 °C for 1000 h. Comparison of the as-grown and

thermally annealed f_{18O} profiles are presented in Fig. 3B. The computed diffusion coefficient (Table 1) of 5.9×10^{-27} m²/s after thermal annealing is smaller than the estimated resolution limit of the APT measurement for this annealing time (D_{limit} ~1.7×10^{-26} m²/s – Fig. 2), indicating no detectable anion diffusion. By comparison, the extracted diffusion coefficients at 500 °C for the irradiated samples range from 2.2×10^{-22} to 4.5×10^{-22} m²/s (Table 1, Fig. 3C), at least 4 orders of magnitude greater than the APT resolution limit of the thermal self-diffusion coefficient and 10 orders of magnitude greater than the Arrhenius extrapolation of higher-temperature literature values. This demonstrates the immense impact of irradiation to accelerate transport in single crystal Cr_2O_3 at temperatures not normally associated with significant anion diffusion.

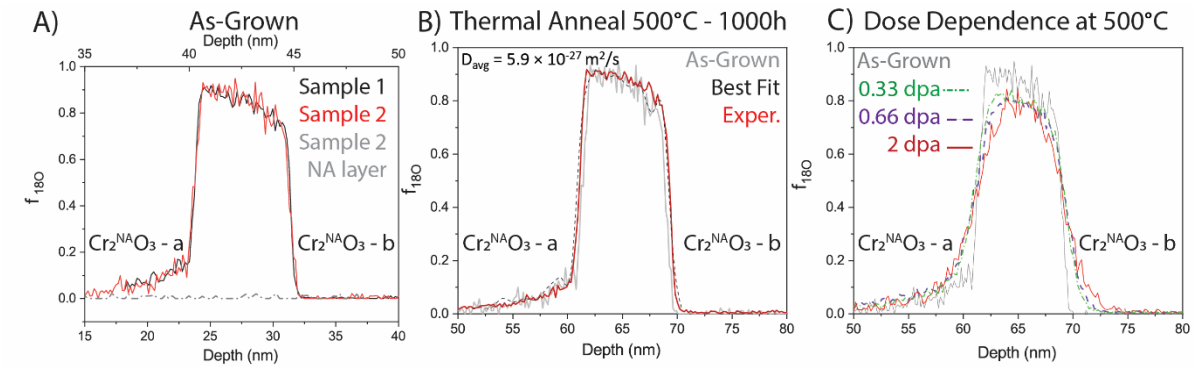

Figure 3. APT-measured f_{18O} profiles for A) as-grown, B) unirradiated, thermally annealed and C) ion irradiated Cr_2O_3 films. The as-grown data show repeatable enrichment profiles from two APT specimens, while the thermally annealed data show no detectable diffusion. Ion irradiation increases anion diffusion to detectable levels, with ^{18}O diffusion increasing at dose. As-grown profile from Sample 2 is included in B) and C) for reference.

Fig. 4 presents APT f_{18O} profiles measured after irradiation at different temperatures. Comparing the extracted diffusivity values reveals a weak temperature dependence at a constant dose of 0.66 dpa. Increasing the irradiation temperature from RT to 500 °C increased the diffusion coefficient

by approximately a factor of 5 (from 6.8×10^{-23} to 3.6×10^{-22} m^2/s). In comparison, extrapolation from literature reports of the high-temperature Arrhenius behavior would predict 46 orders of magnitude lower values at RT,[10] although no experimental data exist in this temperature range for thermal diffusion to confirm this value.

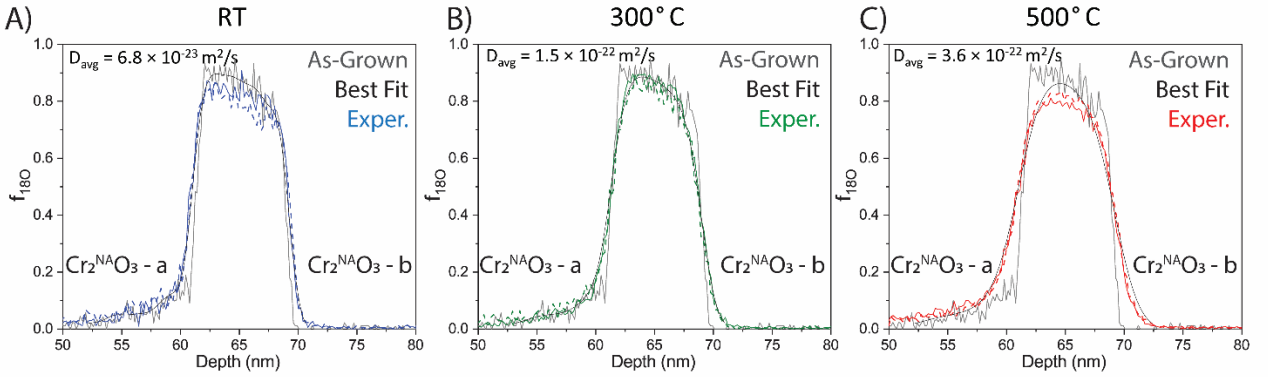

Figure 4. APT-measured f_{18O} profiles after 0.66 dpa irradiations at A) RT, B) 300 °C, or C) 500 °C. The f_{18O} profile broadens with increasing temperature, indicating higher diffusivity values. Each irradiated profile is shown against the as-grown profile (gray), and the best fits from quantifying the diffusivity are shown as solid black lines.

DISCUSSION

Anion diffusivity decreased with cumulative dose, with a consistent reduction in the diffusivity at successive dose levels. That is, the enhanced mobility induced by irradiation was not constant with dose but was enhanced more at lower doses than higher doses. This behavior was analyzed in two ways. First, the average diffusivity up to a given dose was measured by numerically aging directly from the as-grown f_{18O} profile to the best fit of the irradiated f_{18O} profiles. Alternatively, the change in diffusivity with accumulated dose was assessed by extracting incremental diffusivities, for

example by numerically aging the 0.33 dpa or 0.66 dpa f_{18O} profiles to higher dose f_{18O} profiles. These comparisons are presented in Fig. 5A for the incremental (solid circle) and full dose (open square) methods. These diffusivities are also tabulated in Table 1 for the 500 °C irradiations. Both the full dose and incremental analysis show a drop in diffusivity with increasing dose, with the incremental quantification method revealing a larger successive drop in diffusivity. Note that each incremental value uses the preceding dose as reference (i.e. 0.33 to 0.66 dpa, and 0.66 to 2 dpa). A factor of 3–4 reduction in apparent diffusivity is consistent with an associated increase in sink strength with accumulated dose, as visualized by a higher density of larger diameter dislocation loops with dose in Fig. 1. These additional sinks decrease the point defect supersaturation density and depress the associated radiation-enhancement of anion diffusion, although the overall RED effect is still many orders of magnitude greater than what would be expected for thermal diffusion.

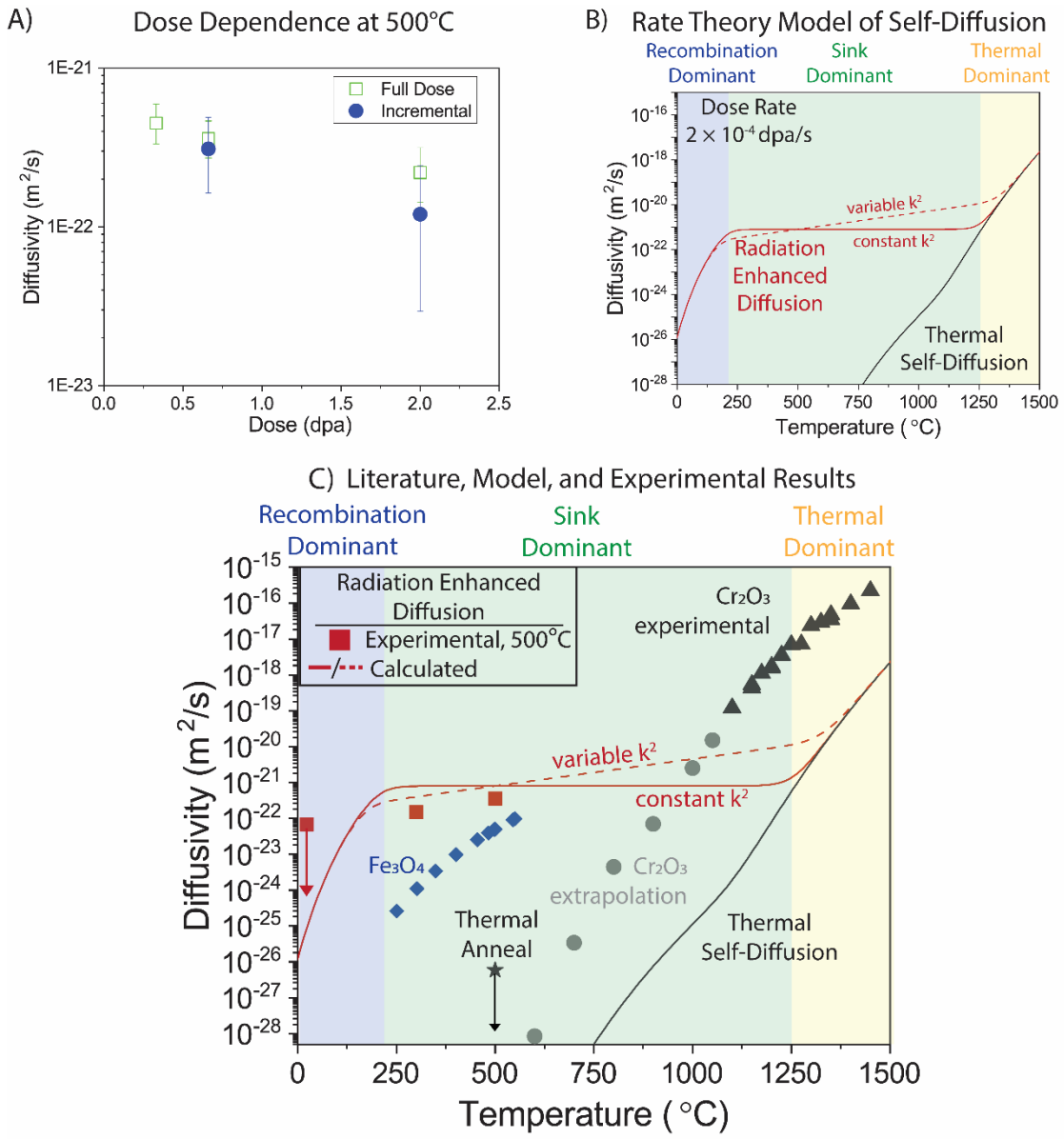

Figure 5. A) Comparison of incremental diffusion coefficient (blue) vs the average full dose diffusion coefficient (purple) at 0.33, 0.66, and 2 dpa, all at 500 °C. The incremental diffusion coefficient drops with increasing dose. B) Chemical rate theory model with thermal self-diffusion curve (black) and radiation enhanced diffusion curves at the experimental dose rate of 2 × 10^{-4} dpa/s for a constant (red, solid) and variable (red, dashed) sink strength (k^2). Three irradiation regimes exist: recombination-dominant at T< 200 °C, sink-dominant at 200 °C < T <

1250 °C, and thermal-dominant > 1250 °C. C) Experimental diffusivity is compared to literature results for Cr_2O_3[10] and Fe_3O_4.[42] Overlaid on the results is the predicted self-diffusion of oxygen by the chemical-rate theory model.

To further understand the underpinnings of the RED in Cr_2O_3, we employ the chemical rate-theory model, developed using Medasani et al.'s[33,34] DFT calculations of defect energetics in Cr_2O_3. Further details on this model are described in SI and ref [22]. The chemical rate theory model enables predictions for both thermal (black) and radiation enhanced (dashed red: variable sink strength, solid red: constant sink strength) conditions, as shown in Fig. 5B. The model predicts that thermal diffusion dominates above ~1250 °C, while defect recombination dominates transport below ~250 °C. In both regimes, the predicted diffusivity is strongly temperature dependent, while at intermediate temperatures (250–1250 °C) anion diffusion is largely temperature-independent. Within this intermediate range, labeled the sink dominant regime, the diffusion enhancement under irradiation depends on two components: 1) production rate of mobile defects and 2) the sink strength. Comparing to the Arrhenius extrapolation from high temperatures confirms that it is the high density of radiation-induced point defects that has increased self-diffusion.

Within the sink dominant regime, the second factor, sink strength, creates additional variability in the predicted diffusivity. Fundamentally, the sink strength is a property of the material microstructure and reflects the average distance point defects must diffuse before being absorbed at a sink. In Fig. 5B, the solid red diffusion curve results from a model that assumes a constant sink strength, resulting in little temperature dependence on the predicted diffusivity. However, as shown by S/TEM images in Fig. 1, the microstructure, and thus sink strength, vary with both dose and temperature. Therefore, calculations using a temperature dependent sink strength in an attempt

to capture the observed microstructural changes were also considered, as illustrated by the dashed red line in Fig. 5B.

Fig. 5C brings together the experimentally measured diffusivities, chemical rate theory model predictions, and reported literature values (measured and extrapolated) for Cr_2O_3[10] and Fe_3O_4[42]. As Fe_3O_4 has higher diffusivity than other Fe oxides, it is used here for comparison as a representative non-protective oxide.[24,27] Comparing the chemical rate theory prediction of thermal diffusivity with data from the literature shows a good general agreement on slope, but with a ~300 °C offset to higher temperature for the model. This offset could be due to the experimental geometry: in the experimental study,[10] all surfaces of spherical particles of single crystal Cr_2O_3 were exposed to 18O. The Arrhenius extrapolation of experimental Cr_2O_3 thermal anion diffusion[10] to 500 °C is off-scale in Fig. 5C (~5×10^{-32} m^2/s) and ~6 orders of magnitude lower than the APT detection limit for a 1000 h anneal (~2×10^{-26} m^2/s). Conversely, the irradiated Cr_2O_3 anion diffusivity at 500 °C (2.2 - 4.5×10^{-22} m^2/s) is ~4–5 orders of magnitude greater than the APT detection limit of the thermally annealed sample. This establishes that irradiation increased the anion diffusivity in Cr_2O_3 by no less than 4 orders of magnitude, and up to 10 orders of magnitude from the Arrhenius extrapolation at 500 °C. This enhancement is equal to or greater than that of grain boundary short-circuit diffusion reported at higher temperatures (850–1100 °C) in chromia (4–5 orders of magnitude faster than bulk)[12,13] and is ~0.5–2 orders of magnitude faster than in unirradiated Fe_3O_4. From the perspective of Wagner-like oxidation kinetics,[43] which are governed by diffusive transport, irradiation will cause Cr_2O_3 (a critical protective oxide) to more closely resemble unprotective Fe_3O_4.

The APT-measured anion diffusivity is in good quantitative agreement with the predictions of the chemical rate theory model, but shows a weak temperature dependence, with a factor ~2.5

difference between the 0.66 dpa at 300 °C and the 0.66 dpa at 500 °C. This suggests that a variable sink strength (Fig. 5C, red dashed line) is more appropriate than a constant sink strength (solid red line), again consistent with the temperature and dose dependence of loop formation shown in Fig. 1. More data on sink (dislocation loop or void) density across a variety of conditions (or, alternatively, a mechanistic model of loop formation in this material) would further improve the sink strength function within the model.

In the recombination-dominant (low temperature) regime, the predicted self-diffusion coefficient drops rapidly. This is caused by accumulation of point defects in the material as the mobility of one species becomes slow enough that it cannot reach a sink before being annihilated by recombination. The mobility of defects decreases with temperature, and at a low enough temperature, long range migration ceases to contribute to self-diffusion. In that regime, atomic rearrangement will be dominated by direct ballistic displacement of atoms during irradiation. This ballistic mixing effect is an athermal contribution to RED which is not included in the rate theory model in this work. The experimental measurements at room temperature - though only just above the resolution limit of our methods – appear to show diffusion on a timescale three orders faster than the model would suggest. This hints that either (a) athermal ballistic mixing is of this magnitude or (b) the defects are more mobile than the DFT calculations suggest. However, given the proximity of the RT data to the resolution limit of the APT, and the very subtle changes in the isotope profile, longer irradiations (roughly 1000 dpa – greater than any reactor component would experience) demonstrating additional transport would be required to draw such a distinction with confidence. Such an irradiation would also likely be complicated by amorphization of the Cr_2O_3 itself, negating any significant further insights into crystalline RED at these temperatures.

CONCLUSIONS

In conclusion, using MBE, S/TEM, and APT, microstructural changes and anion diffusion coefficients were determined after heavy ion irradiation and a comparative thermal anneal of single crystal Cr_2O_3. Irradiation enhances the anion diffusivity at 500 °C by at least 4 orders of magnitude, and likely up to 10 orders of magnitude, from Arrhenius extrapolations of higher-temperature measurements. This radiation enhancement is greatest at lower temperatures. Quantification of the anion diffusion coefficients is also shown to be repeatable across APT specimens by this method. Comparing the experimental results with a predictive chemical-rate theory model, the diffusivity agrees well and demonstrates a weak temperature and dose dependence under irradiation, which can be captured with a temperature-dependent sink strength component. Together, these results highlight the significant increases in transport induced by irradiation and suggest that oxides that are protective against corrosion under thermal conditions may not be protective under irradiation.

ASSOCIATED CONTENT

Supporting Information.

The following files are available free of charge as supporting information.

Figure S1. SRIM generated dose profiles. (image in .doc)

Table S1. Final irradiation times, fluence, and dose for each sample.

Figure S2. Irradiation schematic. (image in .doc)

Figure S3. Cooling curve after 500 °C irradiation. (image in .doc)

Figure S4. Representative mass spectra from Cr_2O_3. (image in .doc)

Figure S5. 16 and 18 Da peaks in the natural abundance Cr_2O_3 vs isotopically labeled Cr_2O_3.

(image in .doc)

Figure S6. Representative bilayer spacing in Cr_2O_3. (image in .doc)

Figure S7. Ball-and-stick model of Cr_2O_3.

Figure S8. Representative 1D concentration profile of APT specimen.

Figure S9. Additional experimental data from dose dependent series.

Figure S10. Spline fits to experimental data used for best fit calculations of experimental runs in Figure 3.

Figure S11. Spline fits to experimental data used for best fit calculations of experimental runs in Figure 4.

AUTHOR INFORMATION

Kayla H. Yano*

*Contact information: kayla.yano@pnnl.gov, (509)-375-2833

Notes

The manuscript was written through contributions of Kayla H. Yano and Aaron A. Kohnert with edits from Daniel K. Schreiber, Tiffany C. Kaspar, Sandra D. Taylor, and Blas P. Uberuaga. Models and fitting were conducted by Aaron A. Kohnert. Sample synthesis was conducted by Tiffany C. Kaspar. APT was conducted by Kayla H. Yano, Sandra D. Taylor, and Daniel K. Schreiber. S/TEM work was conducted by Kayla H. Yano and Steven Spurgeon. The irradiation was conducted by Yongqiang Wang and Hyosim Kim. All authors have given approval to the final version of the manuscript.

The authors declare no competing financial interests.

ACKNOWLEDGMENT

This work was supported as part of FUTURE (Fundamental Understanding of Transport Under Reactor Extremes), an Energy Frontier Research Center funded by the U.S. Department of Energy (DOE), Office of Science, Basic Energy Sciences. A portion of the research was performed using EMSL (grid.436923.9), a DOE Office of Science User Facility sponsored by the Office of Biological and Environmental Research and located at Pacific Northwest National Laboratory. Pacific Northwest National Laboratory is a multiprogram national laboratory operated by Battelle for the U.S. DOE under Contract DE-AC05-79RL01830. This research used resources provided by the Los Alamos National Laboratory Institutional Computing Program. Irradiations were conducted at the Ion Beam Materials Laboratory at Los Alamos National Laboratory. Los Alamos National Laboratory, an affirmative action equal opportunity employer, is managed by Triad National Security, LLC for the U.S. Department of Energy's NNSA, under contract 89233218CNA000001.

REFERENCES

(1) McCafferty, E. *Introduction to Corrosion Science*; 2010. https://doi.org/10.1007/978-1-4419-0455-3.

(2) Beierschmitt, K.; Buchanan, M.; Clark, A.; Robertson, I. Report on Basic Energy Sciences Workshop: Basic Research Needs for Future Nuclear Energy. **2017**.

(3) Weiser, M.; Galetz, M. C.; Chater, R. J.; Virtanen, S. Growth Mechanisms of Oxide Scales on Two-Phase Co/Ni-Base Model Alloys between 800 °C and 900 °C. *J. Electrochem. Soc.* **2020**, *167* (2), 021504. https://doi.org/10.1149/1945-7111/ab69f7.

(4) Chater, R. J.; Carter, S.; Kilner, J. A.; Steele, B. C. H. Development of a Novel SIMS Technique for Oxygen Self-Diffusion and Surface Exchange Coefficient Measurements in Oxides of High Diffusivity. *Solid State Ionics* **1992**, *53–56* (PART 2), 859–867. https://doi.org/10.1016/0167-2738(92)90266-R.

(5) Ooi, T. N.; Mcphail, D. S.; Chater, R. J.; Shollock, B. A. Isotope Exchange Studies of Oxidation Mechanisms in Nickel-Base Superalloys Using FIB-SIMS Techniques. *Surf. Coatings Technol.* **2006**, *201* (7 SPEC. ISS.), 3885–3888. https://doi.org/10.1016/j.surfcoat.2006.07.243.

(6) Falk-Windisch, H.; Malmberg, P.; Sattari, M.; Svensson, J. E.; Froitzheim, J. Determination of the Oxide Scale Growth Mechanism Using 18O-Tracer Experiments in Combination with Transmission Electron Microscopy and Nanoscale Secondary Ion Mass Spectrometry. *Mater. Charact.* **2018**, *136* (December 2017), 128–133. https://doi.org/10.1016/j.matchar.2017.12.001.

(7) Brückman, A.; Emmerich, R.; Mrowec, S. Investigation of the High-Temperature Oxidation of Fe-Cr Alloys by Means of the Isotope18O. *Oxid. Met.* **1972**, *5* (2), 137–147. https://doi.org/10.1007/BF00610841.

(8) Zurek, J.; Young, D. J.; Essuman, E.; Hänsel, M.; Penkalla, H. J.; Niewolak, L.; Quadakkers, W. J. Growth and Adherence of Chromia Based Surface Scales on Ni-Base Alloys in High- and Low-PO2 Gases. *Mater. Sci. Eng. A* **2008**, *477* (1–2), 259–270. https://doi.org/10.1016/j.msea.2007.05.035.

(9) Sabioni, A. C. S.; Lesage, B.; Huntz, A. M.; Pivin, J. C.; Monty, C. Self-Diffusion in Cr2O3 I. Chromium Diffusion in Single Crystals. *Philos. Mag. A Phys. Condens. Matter, Struct. Defects Mech. Prop.* **1992**, *66* (3), 333–350. https://doi.org/10.1080/01418619208201560.

(10) Hagel, Wi. C. Anion Diffusion in A-Cr2O3. *J. Am. Ceram. Soc.* **1965**, *48* (2), 70–75. https://doi.org/10.1111/j.1151-2916.1965.tb11802.x.

(11) Tsai, S. C.; Huntz, A. M.; Dolin, C. Growth Mechanism of Cr2O3 Scales: Oxygen and Chromium Diffusion, Oxidation Kinetics and Effect of Yttrium. *Mater. Sci. Eng. A* **1996**, *212* (1), 6–13. https://doi.org/10.1016/0921-5093(96)10173-8.

(12) Sockel, H. G.; Saal, B.; Heilmaier, M. Determination of the Grain Boundary Diffusion Coefficient of Oxygen in Cr2O3. *Surf. Interface Anal.* **1988**, *12* (10), 531–533. https://doi.org/10.1002/sia.740121005.

(13) King, W. E.; Park, J. H. Anion Grain Boundary Diffusion in Cr2O3 and Cr2O3-0.09 Weight Percent Y2O3. *MRS Proc.* **1988**, *122*, 193–198.

(14) Hoshino, K.; Peterson, N. L. Cation Self-Diffusion in Cr2O3. *J. Am. Ceram. Soc.* **1983**, *66* (11), c202–c203. https://doi.org/10.1111/j.1151-2916.1983.tb10572.x.

(15) Park, J.; King, W. E.; Rothman, S. J. Cation Tracer Diffusion in Cr203 and Cr203-0 . 09 Wt % Y203. *J. Am. Ceram. Soc.* **1987**, *85* (12), 880–885.

(16) Banerjee, A.; Kohnert, A. A.; Holby, E. F.; Uberuaga, B. P. Interplay between Defect Transport and Cation Spin Frustration in Corundum-Structured Oxides. *Phys. Rev. Mater.*

2021, *5* (3), 1–6. https://doi.org/10.1103/PhysRevMaterials.5.034410.

(17) Zinkle, S. J.; Busby, J. T. Structural Materials for Fission & Fusion Energy. *Mater. Today* **2009**, *12* (11), 12–19. https://doi.org/10.1016/S1369-7021(09)70294-9.

(18) Beyerlein, I. J.; Caro, A.; Demkowicz, M. J.; Mara, N. A.; Misra, A.; Uberuaga, B. P. Radiation Damage Tolerant Nanomaterials. *Mater. Today* **2013**, *16* (11), 443–449. https://doi.org/10.1016/j.mattod.2013.10.019.

(19) Cowen, B. Radiation Effects in Metal Oxides and Carbides, 2018.

(20) Nordlund, K.; Zinkle, S. J.; Sand, A. E.; Granberg, F.; Averback, R. S.; Stoller, R. E.; Suzudo, T.; Malerba, L.; Banhart, F.; Weber, W. J.; et al. Primary Radiation Damage: A Review of Current Understanding and Models. *J. Nucl. Mater.* **2018**, *512*, 450–479. https://doi.org/10.1016/j.jnucmat.2018.10.027.

(21) Sickafus, K. E.; Minervini, L.; Grimes, R. W.; Valdez, J. A.; Ishimaru, M.; Li, F.; McClellan, K. J.; Hartmann, T. Radiation Tolerance of Complex Oxides. *Science (80-.).* **2000**, *289* (5480), 748–751. https://doi.org/10.1126/science.289.5480.748.

(22) Yano, K. H.; Kohnert, A. A.; Banerjee, A.; Edwards, D. J.; Holby, E. F.; Kaspar, T. C.; Kim, H.; Lach, T. G.; Taylor, S. D.; Wang, Y.; et al. Radiation-Enhanced Anion Transport in Hematite. *Chem. Mater.* **2021**, *33* (4), 2307–2318. https://doi.org/doi.org/10.1021/acs.chemmater.0c04235.

(23) Dienes, G. J.; Damask, A. C. Radiation Enhanced Diffusion in Solids. *J. Appl. Phys.* **1958**, *29* (12), 1713–1721. https://doi.org/10.1063/1.1723032.

(24) Amami, B.; Addou, M.; Millot, F.; Sabioni, A.; Monty, C. Self-Diffusion in α-Fe2O3 Natural Single Crystals. *Ionics (Kiel).* **1999**, *5* (5–6), 358–370. https://doi.org/10.1007/BF02376000.

(25) Hagel, W. C. Oxygen-Ion Diffusion in Hematite. *Trans. AIME* **1966**, *236* (1), 179–184.

(26) Reddy, K. P. R.; Cooper, A. R. Oxygen Diffusion in MgO and A-Fe2O3. *J. Am. Ceram. Soc.* **1983**, *66* (9), 664–666. https://doi.org/10.1111/j.1151-2916.1983.tb10618.x.

(27) Giletti, B. J.; Hess, K. C. Oxygen Diffusion in Magnetite. *Earth Planet. Sci. Lett.* **1988**, *89* (1), 115–122. https://doi.org/10.1016/0012-821X(88)90037-4.

(28) Kaspar, T. C.; Taylor, S. D.; Yano, K. H.; Lach, T. G.; Zhou, Y.; Zhu, Z.; Still, E. K.; Hosemann, P.; Spurgeon, S. R.; Schreiber, D. K. Bulk and Short-Circuit Anion Diffusion in Epitaxial Fe2O3 Films Quantified Using Buried Isotopic Tracer Layers. *Adv. Mater. Interfaces* **2021**, *2001768*.

(29) Park, S. J.; Seo, M. K. *Solid-Gas Interaction*; 2011; Vol. 18. https://doi.org/10.1016/B978-0-12-375049-5.00002-5.

(30) Thomas, J. M. The Interaction of Gases and Solid Surfaces. *Sci. Prog.* **1962**, *50* (197), 46–64.

(31) Ferro, R.; Saccone, A. Intermetallic Reactivity Trends in the Periodic Table. In *Intermetallic Chemistry*; 2008; Vol. 13, pp 219–318. https://doi.org/10.1016/S1470-1804(08)80006-5.

(32) Taylor, S. D.; Liu, J.; Arey, B. W.; Schreiber, D. K.; Perea, D. E.; Rosso, K. M. Resolving Iron(II) Sorption and Oxidative Growth on Hematite (001) Using Atom Probe Tomography. *J. Phys. Chem. C* **2018**, *122* (7), 3903–3914. https://doi.org/10.1021/acs.jpcc.7b11989.

(33) Medasani, B.; Sushko, M. L.; Rosso, K. M.; Schreiber, D. K.; Bruemmer, S. M. First-Principles Investigation of Native Interstitial Diffusion in Cr2O3. *J. Phys. Chem. C* **2018**, *122* (24), 12984–12993. https://doi.org/10.1021/acs.jpcc.8b04383.

(34) Medasani, B.; Sushko, M. L.; Rosso, K. M.; Schreiber, D. K.; Bruemmer, S. M. Vacancies and Vacancy-Mediated Self Diffusion in Cr2O3: A First-Principles Study. *J. Phys. Chem.*

C **2017**, *121* (3), 1817–1831. https://doi.org/10.1021/acs.jpcc.7b00071.

(35) Thompson, K.; Lawrence, D.; Larson, D. J.; Olson, J. D.; Kelly, T. F.; Gorman, B. In Situ Site-Specific Specimen Preparation for Atom Probe Tomography. *Ultramicroscopy* **2007**, *107* (2–3), 131–139. https://doi.org/10.1016/j.ultramic.2006.06.008.

(36) Ziegler, J. F. Stopping Range of Ions in Matter (SRIM). 2013.

(37) Giannuzzi, L. A.; Stevie, F. A. A Review of Focused Ion Beam Milling Techniques for TEM Specimen Preparation. *Micron* **1999**, *30* (3), 197–204. https://doi.org/10.1016/S0968-4328(99)00005-0.

(38) Zhu, Y.; Ophus, C.; Toloczko, M. B.; Edwards, D. J. Towards Bend-Contour-Free Dislocation Imaging via Diffraction Contrast STEM. *Ultramicroscopy* **2018**, *193* (April), 12–23. https://doi.org/10.1016/j.ultramic.2018.06.001.

(39) Moody, M. P.; Gault, B.; Stephenson, L. T.; Haley, D.; Ringer, S. P. Qualification of the Tomographic Reconstruction in Atom Probe by Advanced Spatial Distribution Map Techniques. *Ultramicroscopy* **2009**, *109* (7), 815–824. https://doi.org/10.1016/j.ultramic.2009.03.016.

(40) La Fontaine, A.; Gault, B.; Breen, A.; Stephenson, L.; Ceguerra, A. V.; Yang, L.; Dinh Nguyen, T.; Zhang, J.; Young, D. J.; Cairney, J. M. Interpreting Atom Probe Data from Chromium Oxide Scales. *Ultramicroscopy* **2015**, *159*, 354–359. https://doi.org/10.1016/j.ultramic.2015.02.005.

(41) Was, G. S. *Fundamentals of Radiation Materials Science*; Springer: New York, 2007.

(42) Castle, J. E.; Surman, P. L. The Self-Diffusion of Oxygen in Magnetite. The Effect of Anion Vacancy Concentration and Cation Distribution. *J. Phys. Chem.* **1969**, *73* (3), 632–634. https://doi.org/10.1021/j100723a025.

(43) Atkinson, A. Wagner Theory and Short Circuit Diffusion. *Mater. Sci. Technol. (United Kingdom)* **1988**, *4* (12), 1046–1051. https://doi.org/10.1179/mst.1988.4.12.1046.